

Public Domain Mark 1.0 Universal

This work was written as part of one of the author's official duties as an Employee of the United States Government and is therefore a work of the United States Government. In accordance with 17 U.S.C. 105, no copyright protection is available for such works under U.S. Law.

Access to this work was provided by the University of Maryland, Baltimore County (UMBC) ScholarWorks@UMBC digital repository on the Maryland Shared Open Access (MD-SOAR) platform.

Please provide feedback

Please support the ScholarWorks@UMBC repository by emailing scholarworks-group@umbc.edu and telling us what having access to this work means to you and why it's important to you. Thank you.

JGR Planets

RESEARCH ARTICLE

10.1029/2023JE007750

Key Points:

- Diurnal air temperature fluctuations measured by Phoenix, Pathfinder and Mars Science Laboratory (MSL) follow solar forcing cycles
- The MSL daytime temperature variance is lower than Phoenix and Pathfinder daytime temperature variances
- Changes in the MSL temperature fluctuations correlate with the seasonal and diurnal timing of pressure drops and dust storm activity

Correspondence to:

E. L. Mason,
emily.mason-1@nasa.gov

Citation:

Mason, E. L., Smith, M. D., Richardson, M. I., & Guzewich, S. D. (2024). Comparing atmospheric temperature fluctuations across landed missions. *Journal of Geophysical Research: Planets*, 129, e2023JE007750. <https://doi.org/10.1029/2023JE007750>

Received 12 JAN 2023

Accepted 21 DEC 2023

Comparing Atmospheric Temperature Fluctuations Across Landed Missions

Emily L. Mason^{1,2,3} , Michael D. Smith² , Mark I. Richardson⁴, and Scott D. Guzewich² 

¹University of Maryland Baltimore County, Baltimore, MD, USA, ²NASA Goddard Space Flight Center, Greenbelt, MD, USA, ³Center for Research and Excellence in Space Science & Technology II, Catonsville, MD, USA, ⁴Aeolis Research, Chandler, AZ, USA

Abstract We analyze and compare atmospheric temperature data from three landed missions: Mars Science Laboratory (MSL) Curiosity rover, Phoenix lander, and Pathfinder lander. Pathfinder and Phoenix were lander missions that operated for 84 and 151 sols, respectively. MSL Curiosity is a rover that operates on the surface of Mars. It has recorded air temperature for more than five Mars Years (MY). We denoise and detrend temperature data from each mission and use those results to calculate variance in air temperature as a diagnostic for atmospheric variability at the surface. The results show a consistent seasonal pattern in MSL air temperature variance with little interannual variability outside major dust storms. The global dust storm in MY 34 was accompanied by a decrease in temperature variance and a muted response in peak MY 35 variance the following year. Phoenix (68°N, 2 m measurement height) and Pathfinder (19.7°N, 1.1 m measurement height) air temperatures have larger variance than air temperature from environmental data records at the MSL location (5.4°S, 1.6 m measurement height) at its equatorial latitude. Pathfinder variances per sol are larger than those of Phoenix, possibly due to a combination of Pathfinder's lower albedo surface and lower latitude. This occurs despite the Pathfinder location's higher thermal inertia, which would act to decrease noontime variance relative to a lower thermal inertia surface. Comparison of MSL temperature variance to pressure drops related to convective vortex activity shows consistent seasonal patterns; however, pressure drops tend to increase with increasing rover elevation, while variance remains consistent.

Plain Language Summary Landed surface missions have collected a long record of meteorological data dating back to the 1970s. Atmospheric temperature, pressure, relative humidity, and winds have been typically measured with each new mission. The atmospheric surface layer consists of the lowest layer of the atmosphere that is directly influenced by the surface. Temperature is a highly consistent measurement and contains signatures of atmospheric surface layer activity in the form of temperature fluctuations. These fluctuations are on the order of seconds to minutes and can be caused by rising thermals, dust devils and convective vortices, changes in wind, and large-scale dynamics. This work compares temperature fluctuations by detrending air temperature data over three missions: the Mars Science Laboratory (MSL) Mission, Phoenix mission, and Pathfinder mission. The results show that these fluctuations change with season and time of day. Greater fluctuations are observed in the afternoon for all three missions and when seasonal insolation is highest. Comparison of MSL temperature fluctuations to pressure drops shows similar trends and decreases during large dust events. However, pressure drops tend to increase over the mission with increasing rover elevation, while temperature variance remains the same with elevation.

1. Introduction

Landed missions on Mars have been successful in sampling the atmospheric surface layer of the Martian atmosphere over the history of Mars exploration. They have provided ground truth to orbital measurements (Smith et al., 2006; Wolff et al., 2006) and serve to elucidate the local geologic and atmospheric environment (see Martínez et al. (2017) for a full review of missions through the landing of Curiosity rover). One of the most common measurements across landed missions is that of near-surface atmospheric temperature. Air temperature data on Mars contain signatures of the atmospheric convection throughout the day within short timescale fluctuations of the order of seconds. These fluctuations persist in length up to half an hour and are indicative of boundary layer behavior at these scales (Davy et al., 2010; Mason & Smith, 2021; Schofield et al., 1997). Wind measurements also contain these signatures (Soria-Salinas et al., 2020; Stull, 1988), and while the wind is normally used for boundary layer similarity and heat flux calculations on a scale of seconds, the lack of available wind data

across most landed missions makes estimation and comparison of surface layer processes difficult. This comparison has been preliminarily attempted using data from the Mars 2020 Perseverance rover Mars Environmental Dynamics Analyzer (MEDA) instrument (Martínez et al., 2023).

Air temperature, on the other hand, is one of the most widely available measurements from landed surface missions, second only to pressure. Temperature contributes to the near-surface activity through thermal contrast between the atmosphere and surface (e.g., Stull, 1988). This drives convection and mixing from below. Convective processes can be much more vigorous on Mars, leading to the formation of a deeper boundary layer than on Earth under similar conditions (Read et al., 2017). Changes in air temperature fluctuations seasonally and diurnally are a proxy for the strength of convection and mixing. Therefore, to diagnose the behavior of the boundary layer on seasonal and diurnal scales, it is beneficial to use temperature to assess the changes in the surface layer through periods of varying forcing (Mason & Smith, 2021).

Near-surface air temperature data are available for all landed missions, but temporal resolution and quality vary across each data set. Both Viking landers carried meteorological packages (Soffen & Snyder, 1976). The landers collected high-frequency measurements of temperature and pressure (e.g., Chamberlain et al., 1976) but subsequently averaged the resulting temperature, making the comparison of short-term fluctuations infeasible for this study. The Pathfinder (Schofield et al., 1997) and Phoenix (Taylor et al., 2008) lander missions both measured higher latitude meteorological processes at 19° and 68°N, respectively. The missions were separated by about five Mars Years (MY). Their data sets, while short-lived in mission length, provide well-calibrated and consistent measurements of air temperature at frequencies of 0.5 Hz for Phoenix and up to 1 Hz for Pathfinder. Though the Mars Exploration Rover missions did not carry dedicated meteorological packages, surface and air temperatures were derived using the Miniature Thermal Emission Spectrometer instrument (Smith et al., 2006; Spanovich et al., 2006), which has proved useful in analyzing vertical responses within the boundary layer (Mason & Smith, 2021).

Equatorial missions that continue to provide high-quality data for temperature and pressure are now operating on the surface. These include the Mars Science Laboratory Mission (MSL's rover, also called "Curiosity") (Grotzinger et al., 2012), which is one of the longest running missions on the surface of Mars. The meteorological data set that it provides is exceptional due to its record length. In addition to Curiosity, there are two other NASA missions recently in operation: InSight (Banfield et al., 2020), and Mars 2020 Perseverance Rover (Farley et al., 2020; Rodriguez-Manfredi et al., 2023). Both missions include instruments capable of measuring temperature at frequencies greater than 1 Hz; however, because these are newer missions, and because their analysis requires more detailed attention (Munguira et al., 2023), we do not include those missions in this work. For this analysis, we chose to compare the MSL, Phoenix, and Pathfinder missions at three different latitudes and within different topographic regimes and Mars Years. While views of seasonality are limited to interannual variability in the temperature data for MSL, diurnal variability is comparable across these missions.

The work is presented in the following format. Section 2 discusses each mission location and air temperature data set. Section 3 describes the basic techniques used to analyze the data and details the uncertainty with each data set. Section 4 shows statistical and frequency results using the methods described in Section 3, and Section 5 discusses possible physical processes that are responsible for the results presented in Section 4. Finally, Section 6 presents the conclusions of this work.

2. Data

The work presented here focuses on three missions: The MSL Curiosity Rover, the Phoenix lander, and the Pathfinder lander mission. All three missions produced atmospheric temperature data using in situ measurements from meteorological payload packages. Data were processed for this work according to the methods outlined in Sections 3.1–3.3.

Air temperature data have been published for each mission and a full review of meteorological variables can be found in Martínez et al. (2017). Here, we show air temperature in Figure 1 for reference. Air temperature for the three missions ranges from a low of 175 K at the Phoenix landing site to approximately 290 K at the Curiosity rover location. Gaps in the data shown in Figure 1 represent times of conjunction and temporary pauses in operation to manage mission power (e.g., Figure 1a, MY34, $L_s \sim 180^\circ$ following the onset of a global dust storm). Phoenix operated nearly continuously over its entire mission timeframe, pausing only briefly near noon each sol

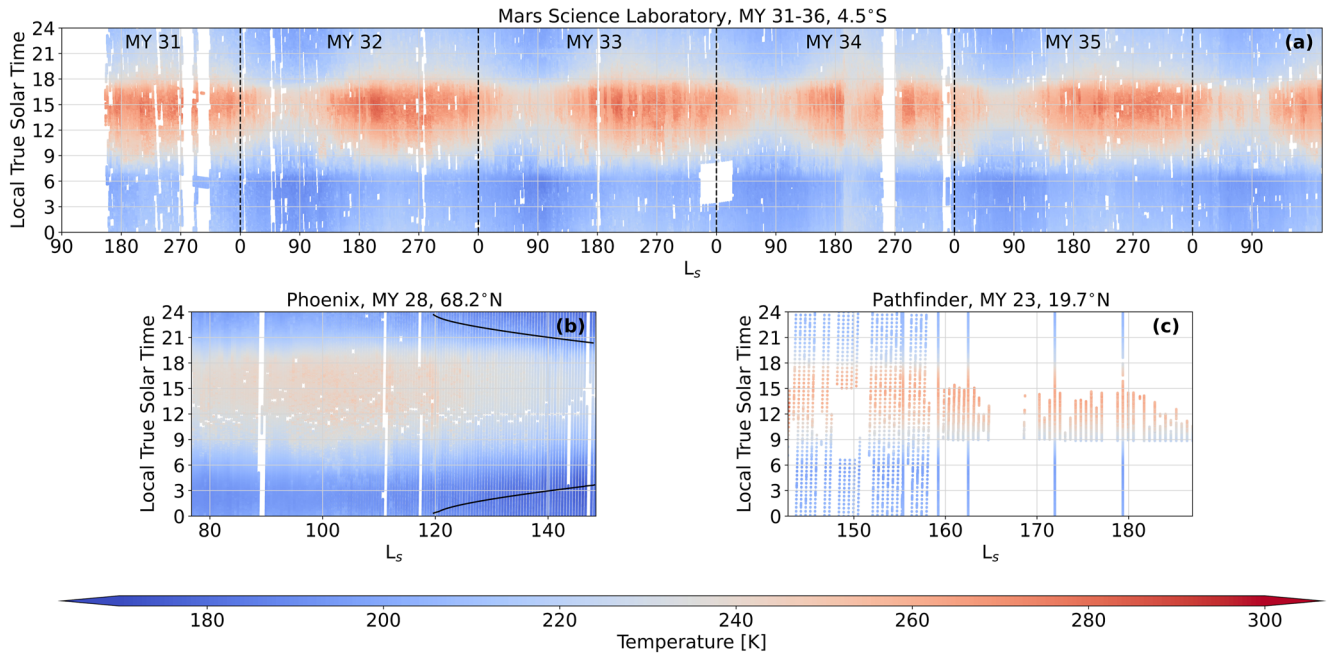


Figure 1. Air temperature data as a function of solar longitude (L_s) and local true solar time for (a) Mars Science Laboratory Rover Environmental Monitoring Station, (b) Phoenix Meteorological Station (MET), and (c) Pathfinder Atmospheric Structure Investigation/Meteorology Package (ASI/MET). The black solid lines in panel (b) represent times when the sun was below the horizon. Dotted vertical lines in panel (a) mark MY transitions.

to store data and at times when power was low. As described in Section 2.3, Pathfinder collected data at lower frequencies for short periods of time to observe entire sols.

Air temperature for the MSL and Phoenix missions follows the expected seasonal patterns for the respective locations, where maxima in seasonal temperature correspond to northern and southern hemispheric summers. Changes due to seasonality in Figure 1b are also obvious despite the shorter operational time. For Phoenix, air temperatures quickly diminish following the setting of the sun, which is marked by the black lines in Figure 1b. In addition, diurnal patterns are apparent in all three sets of mission data, showing the typical maximum at roughly $\sim 15:00$ local true solar time (LTST) for measurements made 1–2 m above the surface. Decreases in atmospheric temperature are noticeable in the MY 34 daytime air temperatures in Figure 1a after $L_s \sim 180^\circ$ due to a global dust storm (e.g., Guzewich et al., 2019).

2.1. Pathfinder ASI/MET

Pathfinder was a NASA Discovery class mission that placed a lander on the surface with an accompanying Sojourner rover. The lander carried the Imager for Mars Pathfinder and the Atmospheric Structure Instrument/Meteorology package (ASI/MET) (e.g., Schofield et al., 1997). Pathfinder arrived 4 July 1997, in the Ares Vallis region at 19.3°N and 33.21°W longitude and operated for a short lifetime (84 sols). The surface properties of the higher elevation region consisted of higher thermal inertia and lower albedo compared to other locations on Mars. From TES global thermal inertia maps (Putzig & Mellon, 2007), the thermal inertia near the Pathfinder lander was greater than $386 \text{ J m}^{-2} \text{ K}^{-1} \text{ s}^{-1/2}$ and the albedo derived from Viking Infrared Thermal Mapper observations ranged from 0.19 to 0.23 (Edgett & Christensen, 1997). Based on modeling, the maximum mid-sol solar irradiation at the surface during the mission was close to 600 W m^{-2} .

Fast response temperature sensors were located on the lander petals at 1.1 m (Schofield et al., 1997). The sensors had an accuracy of $\pm 1 \text{ K}$ and a resolution of 0.04 K (Martínez et al., 2017) with a corresponding time constant of 4–5 s (Seiff et al., 1997) at a wind speed of 1 m s^{-1} . Available data (Murphy, 1999) include measurements at a rate of 0.25 Hz for the first 25 sols in 51 equally spaced segments with higher frequency (1 Hz) sessions of 15 min and 1 hr. Following that point, more regular, lower-frequency observations at 0.25 Hz were taken to assess air temperature across an entire sol. The temperature sensors were located on a mast on the edge of the lander

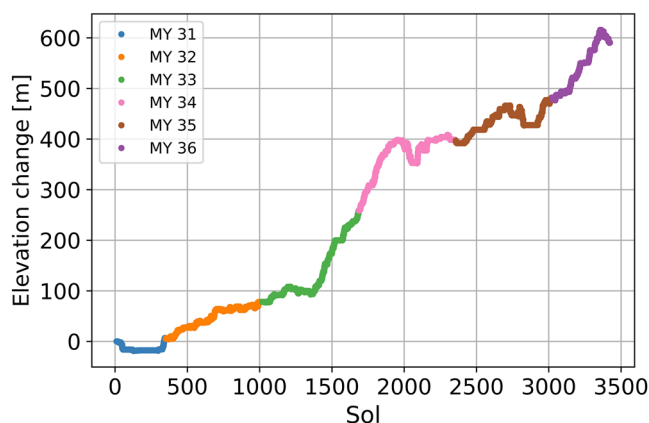


Figure 2. Elevation change as a function of mission sol for the Curiosity rover. Each subsequent MY is highlighted with a different color. Changes between MY 33 and 34 represent the largest gain in elevation, which includes the time Mars Science Laboratory crossed the Bagnold dune fields.

petals so that interference from the lander was minimized. Many of the observational periods at the beginning of the mission lasted less than 5 min, but because the Pathfinder mission had such a short lifetime, we have included those observational periods in our analysis of air temperature variance. To calculate fluctuation durations, as discussed in Section 3.3, we excluded these shorter observational periods.

2.2. Phoenix MET

The Phoenix lander was stationed at 68°N, 106°W in a homogeneous plain of regolith-water ice mixture with moderate thermal inertia. Studies prior to landing estimated thermal inertia of potential landing sites to be near $200 \text{ J m}^{-2} \text{ K}^{-1} \text{ s}^{-1/2}$ (Bandfield, 2007), while the albedo was estimated to fall within 0.15–0.3 (Putzig & Mellon, 2007). Elevation was low and maximum surface solar irradiance was less than 400 W m^{-2} . The lander, which ceased operations only 151 sols after it began, was a short but successful mission designed to characterize the polar environment (Taylor et al., 2008). Its deployment on the polar surface provided atmospheric temperature and optical depth among other measurements in a location that is still unique to this day.

Fast response air temperature sensors were located on a Remote Sensing Mast (RSM) at heights of 0.25, 0.5, and 1 m above the lander solar panels, which stood another 1 m off the ground (e.g., Taylor et al., 2008). Because of interference from the lander, estimated up to 1 K (Davy et al., 2010), only data from the highest sensor is used in this analysis. This minimizes the effect of thermal plumes on the air temperature signature. Air temperature data (Dickinson, 2008) were collected at a frequency of 0.5 Hz at most times during the day. The near-continuous nature of measurements is one that is extremely beneficial to this study, as it allows us to see the entire sol even if higher frequency fluctuations cannot be observed.

2.3. Mars Science Laboratory REMS Instrument

The MSL mission has long surpassed its operational goal, and in doing so has provided the longest running surface meteorological data set on Mars (Vasavada, 2022). Since landing in Gale crater (5.4°S, 137.8°E) the rover has traversed more than 25 km and gained over 600 m of elevation (Guzewich et al., 2021; Vasavada, 2022), with the largest elevation gain of ~200 m occurring at the end of MY 33 and the beginning of MY 34 (see Figure 2). Mount Sharp extends through 5,500 m to its peak. This is almost equivalent to Denali Mountain in Alaska, United States, which extends just over 6,000 m. In addition, the rover sits in a crater of about 1 km in depth. The traverse of the rover within Gale Crater and onto the slopes of Mount Sharp is unique to landed missions thus far. Throughout the mission, Curiosity has moved through different topographical terrains, elevations, and thermal surface conditions (see Figure 1 from Vasavada (2022)), including the Bagnold Dunes in MY 32, where conditions were favorable for the development of dust devils and convective vortex activity (e.g., Newman et al., 2019).

Analysis of the thermal inertia in the region using CRISM-based high spatial resolution images shows variable surface properties along the traverse (Christensen et al., 2022) with the lowest values in the dunes reaching just over $100 \text{ J m}^{-2} \text{ K}^{-1} \text{ s}^{-1/2}$ and the highest values along the ridge surpassing $400 \text{ J m}^{-2} \text{ K}^{-1} \text{ s}^{-1/2}$. However, portions of the traverse fall within regions of surface having thermal inertia in the range of $300\text{--}400 \text{ J m}^{-2} \text{ K}^{-1} \text{ s}^{-1/2}$ (Vasavada et al., 2017). Additional estimates from Martínez et al. (2021) show thermal inertia derived from surface energy balance ranging from ~150 to 620 SI units and albedo ranging from 0.05 to 0.3.

Daily meteorological observations consisting of air temperature, pressure, relative humidity, and ultraviolet (UV) irradiance are collected using Rover Environmental Monitoring Station (REMS) (Gómez-Elvira et al., 2012, 2014). Two booms situated on the RSM measure local air temperature at 1.6 m, while the UV and pressure sensors are located on the body of the rover (Gómez-Elvira et al., 2012). Surface skin temperature is measured using thermopiles that detect infrared radiation mounted on the RSM and pointed downward. These are subject to larger electronic noise at nighttime air temperatures but provide an estimate of the boundary layer regime during a diurnal cycle with respect to air temperature (e.g., Martínez et al., 2017). The baseline cadence

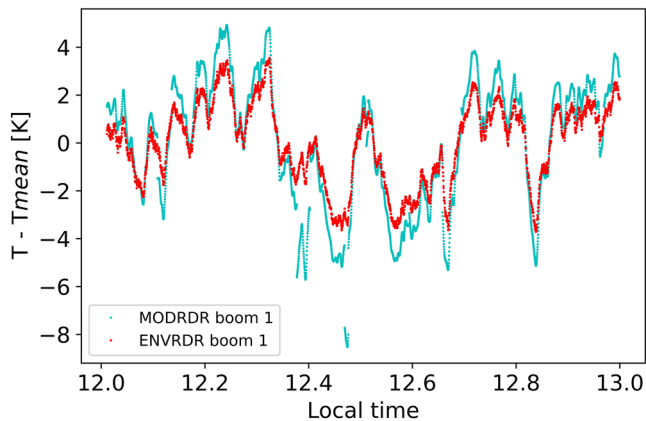


Figure 3. Mars Science Laboratory mission sol 3068 (MY 36, $L_s = 22^\circ$) around local noon showing Modeled Reduced Data records (modeled) data products from boom 1 compared to the Environmental Magnitudes Reduced Data Records (local) data products for tip air temperature from boom 1.

of observations occurs in five-minute intervals at 1 Hz frequency. Extended blocks consisting of one to 5 hr of data are also collected at the same frequency in a rotating schedule that repeats every few sols. In this way, high-frequency measurements are captured over the full sol, though more frequently at some hours than others. In addition, the solar noon hour is routinely covered with a single extended block. Flags, which are binary values indicating whether the measurement was taken within certain favorable conditions, are carried through from the data products. These include indicators of when the rover was in motion as well as when the sensors were covered in shadow. We also mark each observation as one that exists within an extended block or in a 5-minute cadence block. In this way, we work directly with extended block measurements and disregard the five-minute blocks.

For this study, we selected meteorological variables from multiple data products. Pressure and air temperature are gathered from the Modeled Reduced Data records (MODRDR) (Gómez-Elvira, 2013c) and Environmental Magnitudes Reduced Data Records (ENVRDR) data products (Gómez-Elvira, 2013b), respectively, and combined with ancillary information, including rover position, solar position, and seasonal insolation.

ENVRDR files contain calibrated physical readings and represent air temperature in the local vicinity of the rover. Modeled temperature data products from the MODRDR files are decimated to 0.1 Hz (e.g., Miller et al., 2018).

Air temperatures used in this analysis are restricted to boom 1 tip temperatures (Gómez-Elvira et al., 2012; Miller et al., 2018) within the ENVRDR products (see Figure 3 for an example of air temperature from both the MODRDR and the ENVRDR data sets). This is because modeled ambient air temperatures contained in the MODRDR files are decimated to a frequency of 0.1 Hz and the local boom 2 air temperatures contain wide swings that are not representative of atmospheric temperature. An example of the difference between the boom 1 ENVRDR products and the boom 1 MOD products is shown in Figure 3, where the magnitudes of the air temperature fluctuations are larger than those of the ENVRDR boom 1 tip air temperatures. This is because the response time for the MSL REMS temperature sensors is slower than that of Phoenix and Pathfinder (Gómez-Elvira et al., 2014). The slower response time convolved over the actual changes in the air temperature produces a muted response and acts as a low-pass filter. Despite the differences, structures present in both temperature data types are apparent past the noise limit of the instrument (see Figure 4, right column distributions). These structures are directly comparable to those seen in the Phoenix and Pathfinder air temperatures. Results between the modeled and ENV do not affect the seasonal and diurnal patterns, but only the magnitudes in the variance. Differences between the magnitudes can range from 0 to 4 K. We assume that the boom 1 tip air temperatures are representative of local atmospheric changes and represent a low estimate of the fluctuations. In addition, signatures within the air temperature data can sometimes be attributed to non-atmospheric sources. The two major contributors are instrument noise and heat plumes from the Radioisotope Thermal Generator (RTG) that powers the rover (see Section 3). Shadows over the air temperature sensor from the RSM can also influence the measured signal, but because these occur over much longer scales than those analyzed here, we consider this negligible.

3. Methods

Characterization of surface layer behavior can be assessed using a combination of statistical and frequency analysis tools (Stull, 1988). The former provides a measurement of atmospheric variability at the surface, which includes turbulent intensity, of the selected meteorological variables, and the latter provides insight into the durations of atmospheric thermal structures.

3.1. Statistical Analysis

The simplest method to determine the intensity of atmospheric variability at the surface is by taking the hourly variance (the standard deviation squared) of the difference between a running mean curve and the denoised air temperature data set. Subtracting a running mean from the local air temperature over each sol serves to

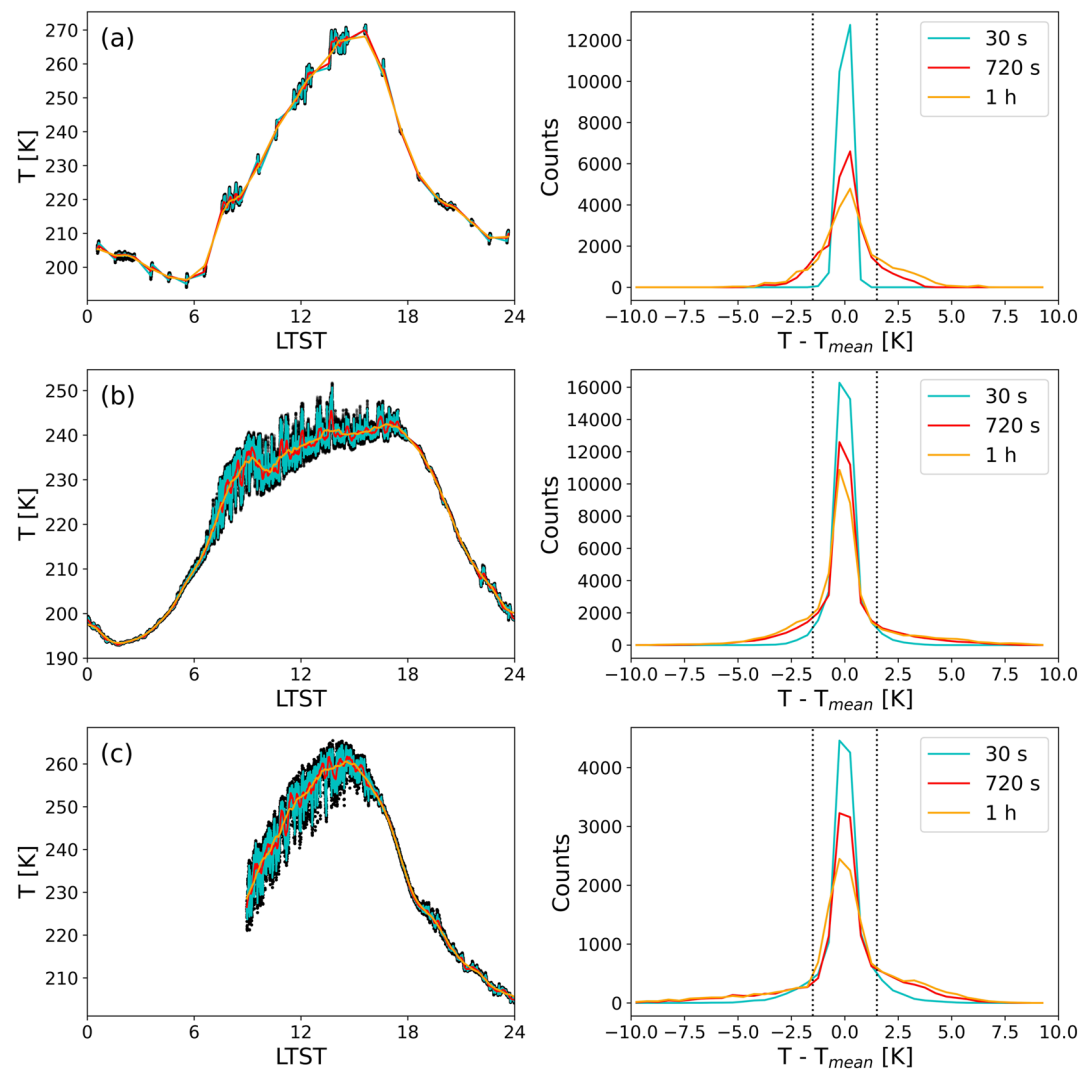


Figure 4. For each sol of each mission, temperature is detrended using a running mean of varying window sizes (30s, 720s, and 1 hr). Three running mean results are shown in the left column of this figure for a selected sol of (a) Mars Science Laboratory, (b) Phoenix, and (c) Pathfinder. These are plotted with temperature. The resulting distribution function in the right column shows the change in deviations with each running mean. Higher running means sample larger convective structures and atmospheric phenomena. Colors in the right columns correspond to running means in the left columns. Vertical lines in the right column correspond to a fluctuation magnitude of 1.5 K.

detrend the data and removes the large-amplitude diurnal and long-duration signatures. The resulting difference after subtracting the running mean from the original data for each sol highlights fluctuations on the order of seconds to minutes (Davy et al., 2010; Mason & Smith, 2021; Tillman, 1972). These short-timescale fluctuations in air temperature are indicative of activity within the surface boundary layer. Figure 3 shows an example of the detrended MSL temperature over 1 hr. Figure 4 shows examples of the running mean and the resulting distributions.

To find a consistent method for determining the mean profile, three different running means were tested on several sols of air temperature data from each mission. Figure 4 shows an example of a single sol for Phoenix, Pathfinder, and MSL. This experiment was also performed in a previous work by Davy et al. (2010) to show how the choice of running mean affected the resulting fluctuation magnitude and statistics. In a similar fashion, we tested running means of 12 min and 1 hr to see the changes in the statistical measurements. The right panel of Figure 4 shows the distribution of the resulting detrended temperature for each choice of running mean. For MSL air temperature data, we include the 5-min blocks to calculate the running means but do not include them

when calculating variance. The profiles in Figure 4 show the distribution of air temperature for these two selected running means along with the 30-s running mean used to remove noise (see Section 3.2).

Statistics for the 1-hr running mean and the 12-min running are not significantly different. In general, the longer the window size for a running mean, the larger the resulting skew and variance. For consistency, we choose a running mean of 12 min to compare directly to previous work (e.g., Davy et al., 2010). Longer duration signatures could include processes not associated with free and forced convection, including gravity waves. However, by limiting our analysis to structure durations less than 30-min, we are not looking at large-scale influences. Guzewich et al. (2021) looked for waves within the air temperature data on timescales of minutes to hours and did not find signatures like those found in the pressure data. The shapes of the running mean curves used here are sufficient to diagnose the behavior of convection on a diurnal and seasonal cycle regardless of the choice of running mean.

3.2. Instrument Noise versus Atmospheric Events

We considered two major contributors of non-atmospheric fluctuations in the REMS data: the RTG, which can be significant source of heat up to 4 K in the GTS data (Martínez et al., 2017), and internal instrument noise (e.g., Miller et al., 2018; Zurita-Zurita et al., 2020). MSL REMS temperature fluctuations are smaller than those of Pathfinder and Phoenix temperature fluctuations, especially when viewing the local ATS boom 1 tip air temperatures, and therefore estimation of the noise level is important at all local times over a sol.

Instrument noise is evident in the root mean square (RMS) of temperature fluctuations within the REMS temperature ENVRDR data set (Figure 5a). The MSL RMS for MY 32 was compared to the RMS for Phoenix and Pathfinder in Figures 5c and 5e, respectively. Taking the entire MY 32-air temperature record, for example, we calculated the RMS for each 30-min interval in local time. The lowest RMS for this MY is ~ 0.6 K during the nighttime hours (see Figure 5a). However, Miller et al. (2018) showed that the second-to-second variations in temperature could be large at night, up to 1.5 K. This can be seen in calculations of second-to-second changes in temperature reproduced in Figure 5b, where a minimum threshold of 0.6 K has been set to show variations larger than what is determined for the nighttime RMS. The diurnal shape of these second-to-second changes does not follow what is expected of a typical atmospheric response, which would consist of higher mid-sol variation seen using fast-response sensors. This is why the second-to-second changes for the Pathfinder and Phoenix temperature data in Figures 5d and 5f have different diurnal patterns than that of the MSL shown in Figure 5b. There is also a distinct seasonal effect, shown in Figure 5b, that is present in MSL air temperature fluctuations. This is because the operational conditions of the temperature sensors are not always ideal. For instance, noise at nighttime is higher than during the day and is also higher in southern hemispheric winter when the temperature is lower than during southern summer. As seen in both the RMS values and the second-to-second variations in Figure 5b, the noise level for the MSL REMS temperature data is highest at night and during the southern winter season. This is expected, and variance falling within this noise range can be approached carefully.

As the running mean window increases, at some point, the diurnal pattern of temperature deviation shifts from one that is indicative of noise to a diurnal pattern that is more representative of atmospheric fluctuations. This happens when the noontime variance is higher than the nighttime variance. In Figure 6, this result is shown in the difference between the green and magenta curves. Reducing the window size of the moving average brings the distribution of fluctuations closer to a Gaussian shape (see Figure 4, right panels). We use this diurnal dependence to our advantage by applying a moving average of small window length to the temperature data prior to detrending, as was done in Miller et al. (2018) using a Fourier transform. Prior to calculating the variance, we applied a 30-s moving average to de-noise the air temperature data. We then calculate the fluctuations and variance by detrending with a running mean of 720 s. We then used extended hour blocks to calculate the variance, removing the 5-min observations.

We do not try to remove instances where there might be a significant contribution from the RTG. These instances occur in less systematic bursts that are dependent on the rover and wind direction and cannot be accurately determined without a measurement of both. They are therefore folded into our analysis under the assumption that they do not occur as often as real atmospheric events on the scales we are interested in viewing. We adopt an uncertainty in fluctuations of 1 K, which is a conservative estimate that falls between the lowest calculated RMS and that of previous work.

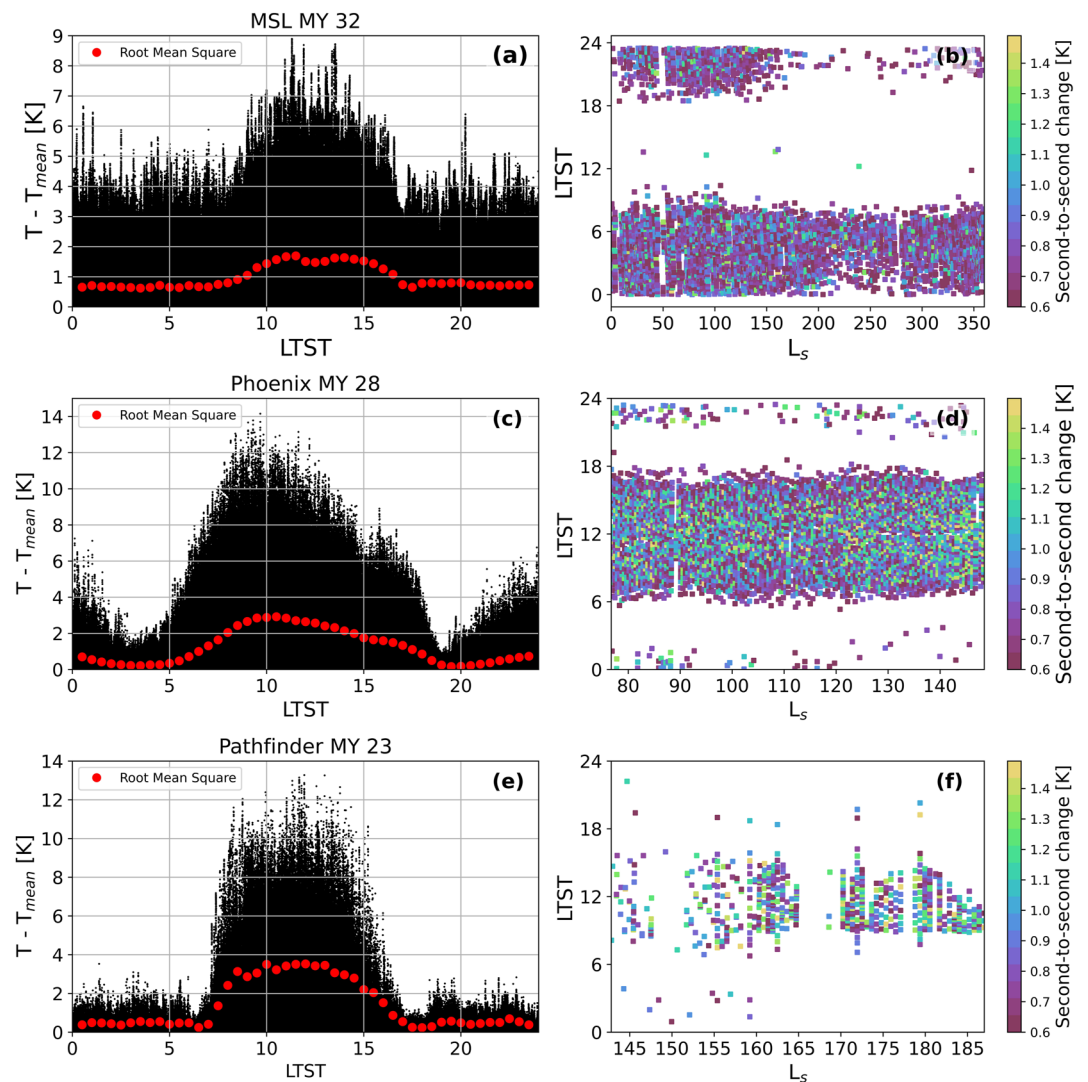


Figure 5. Detrended air temperatures for all sols are plotted for each mission in the left column, and the root mean square (RMS) is calculated in bins of 30 min. Second-to-second variations in temperature are shown in the right column. (a) Shows all air temperature fluctuations for Mars Science Laboratory (MSL) MY 32 in black and the 30-min binned RMS of all fluctuations for MSL MY 32 in red. (b) Seasonal dependence of second-to-second changes in air temperature. The middle and last rows show the same results in panels (a, b) for Phoenix and Pathfinder, respectively.

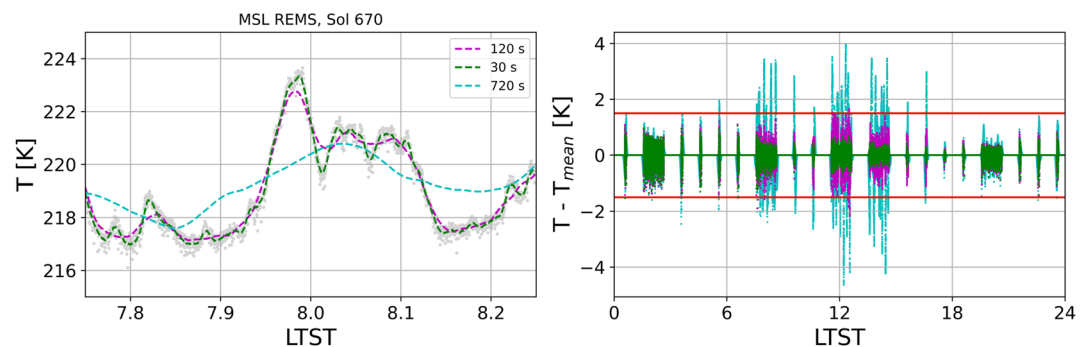


Figure 6. An example curve in the left panel shows running means against a subset of air temperature data for sol 670. Diurnal fluctuations are shown in the right after subtracting each running mean shown in the left panel. Noise is apparent in the detrended data using a running mean of 30 s.

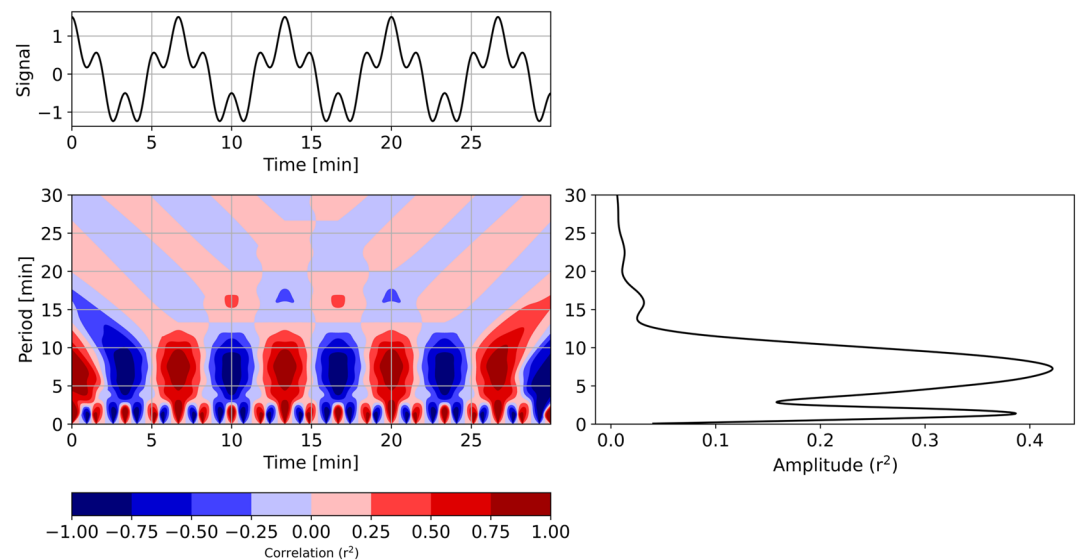


Figure 7. Idealized example of the cosine correlation technique with strong correlations to periods at 100 and 400 s (1.6 and 6.6 min). A more realistic example is provided in Mason and Smith (2021).

While both Phoenix and Pathfinder temperature data contain this type of noise, the magnitude of the temperature fluctuations in the data is larger than the 1 K accuracy limits of the instruments. This becomes important only at night for both missions, when nighttime fluctuations are indicative of active atmospheric processes (Schofield et al., 1997; Zent et al., 2016). Davy et al. (2010) estimate that influences from the lander are on the order 1–2 K. Since we are only interested in the diurnal cycle, we adopt the 1 K estimate for noise for both Phoenix and Pathfinder as well.

3.3. Frequency Analysis

While variance can be a measure of intensity, it does not provide information on the shapes of atmospheric structures. Structures and their durations within the air temperature data provide an understanding of seasonal activity without relying on fluctuation magnitude. While magnitude is subject to noise and convolution from sensor response times, frequency analysis views the durations of the signatures alone, dividing out the magnitude of each signature. For this, frequency analysis is a useful tool. We use the method described in Mason and Smith (2021). The method takes one half of a cosine function with a set period and correlates that function to segments of the detrended air temperature signature with the same period. Figure 7 shows an example of this method for a simple curve with two different wave contributions. The partial cosine curve is convolved over the signal using periods ranging from seconds to 30 min, and the correlation between the two curves is calculated. The amplitudes are calculated by taking the square of the correlations, and these amplitudes are averaged across the entire time block. In the case of air temperature, this is done in 1-hr increments. The resulting curve shows higher amplitudes for the periods that are present in the signals. The amplitude changes with the fluctuation magnitude of each contribution. We show the results for this application in Section 4.

4. Results

We present statistical and frequency analysis results for MSL, Phoenix, and Pathfinder, covering MY 23 through MY 36 (with gaps). The data represent a view of the seasonal and diurnal changes in boundary layer activity at each site and show how this activity differs between location and terrain. All variance results are shown in Figure 8 as hourly bins. Note that there is a different scale used for MSL compared to Phoenix and Pathfinder. Places where observations do not exist are colored in white.

4.1. Temperature Variance

Temperature variance for the MSL mission (see Figure 8a) shows both seasonal and diurnal patterns that follow diurnal solar irradiance. Results are given for all data available through the first half of the MY 36. Within

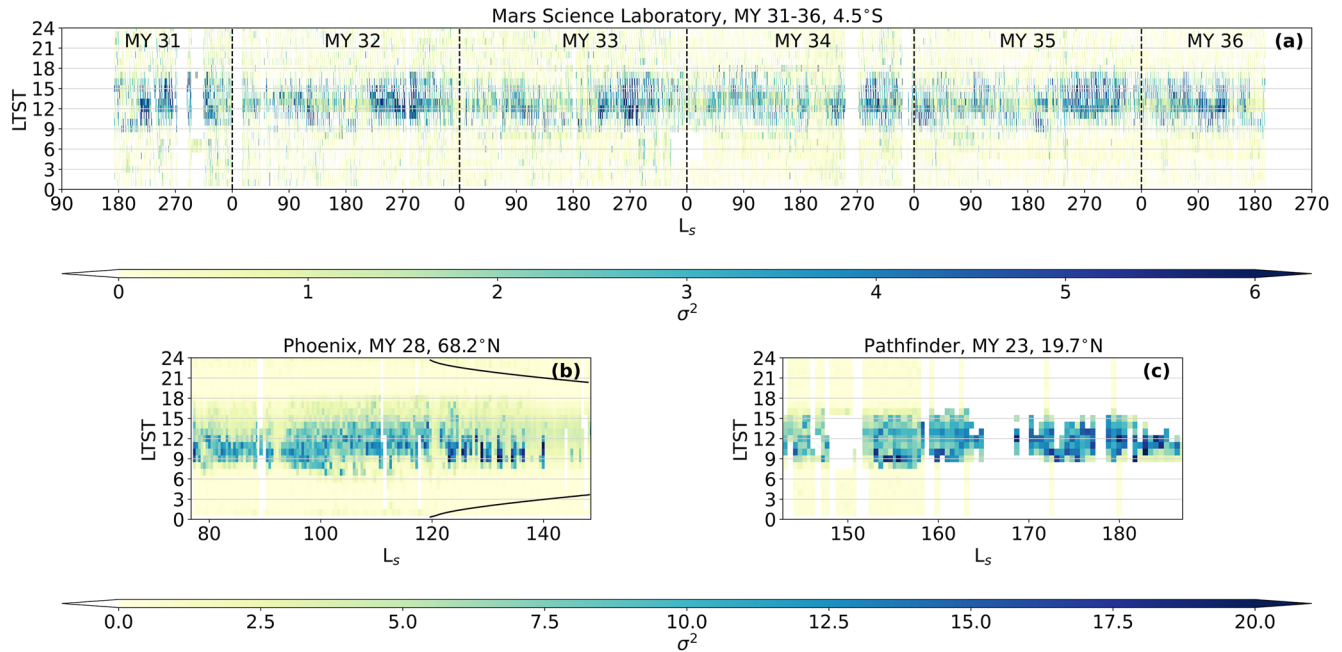


Figure 8. Hourly mean-binned variance for (a) Mars Science Laboratory Rover Environmental Monitoring Station, (b) Phoenix MET, and (c) Pathfinder Atmospheric Structure Instrument/Meteorology package air temperatures.

Figure 8a, the highest variances ranging from 6 to 8 K² tend to fall near the southern hemisphere solstice (L_s ~ 270°), which is a repeated pattern for each MY. In addition, there tends to be a secondary local maximum near the northern summer solstice, L_s ~ 90°, which is closer to the aphelion. This local maximum is also evident in most MYs. Decreases in variance for MSL are evident during large dust storm events, consistent with previous observations (Ryan & Henry, 1979). This is best seen for the global dust storm in MY 34 just after L_s ~ 180° (Guzewich et al., 2019) and can also be seen in MY 36 near L_s ~ 140° when a large regional dust storm passed over the rover's location (Smith et al., 2023). Equinoctial periods tend to exhibit lower variance, with a minimum existing near L_s = 180°. The diurnal structure at MSL is consistent with the results of Guzewich et al. (2021), showing an increased activity during the day, a quiet period just before 18:00 LTST, and lower nighttime activity. Values for the standard deviation, that is, the square root of the variance, are on average about 1–3 K and are in line with statistical values presented in Miller et al. (2018) and Guzewich et al. (2021) (see Figure 7 of Guzewich et al. (2021)) despite using different detrending methods.

Nighttime variance, defined as that falling between the hours of 18:00 and 06:00 LTST the following sol, is generally small and less than 1 K² for MSL. Instances of variance larger than 1 K² can be seen in the hours of 18:00 to 23:00 LTST and again in the early morning hours of 01:00 to 05:00 LTST. This increase is only evident for the first three MY of the MSL mission and tends to decrease in MY 34, 35, and 36. Nighttime variance during these last MY's tends to be stronger during southern hemispheric summer. Maxima in the binned diurnal variance for all MY peak after 12:00 LTST, in line with the peak in atmospheric temperature (Figure 1a).

Compared to MSL, Phoenix variance in Figure 8b is larger. Values of 1–20 K² are observable, corresponding to fluctuations of 1–5 K on average. Fluctuations up to 20 K have been observed within the data (Holstein-Rathlou et al., 2010). The seasonal trend of Phoenix is still visible despite its short lifetime. Phoenix operated from northern spring (L_s ~ 76°) to northern summer (L_s ~ 148°) before ceasing operations. The variance, much like the temperature, increased during this time, peaked mid-season, and then fell again. The black lines in Figure 8b represent sunset at the Phoenix location. The sun did not fall below the horizon until about sol 90. Variance and temperature showed a strong diurnal signature, in line with changes in the solar irradiance. Toward the end of the mission, when air temperatures were lower and the nights were longer, variance also decreased. Prior to L_s = 140°, variance exhibited strong changes, with peaks in the morning and decreases in the afternoon. Later in the season, the morning variance strengthened. Early mission dust events are attributed to sublimate the CO₂ ice caps, which do not coincide with changes in wind speed and direction (Holstein-Rathlou et al., 2010).

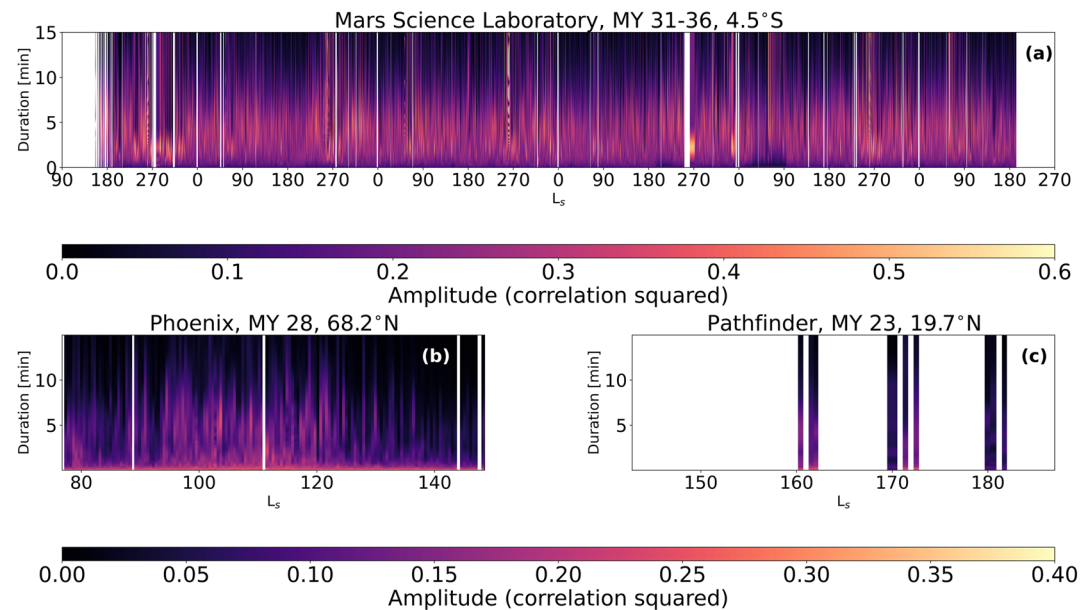


Figure 9. Correlations of temperature fluctuations with partial cosine curves between 12 p.m. Local true solar time (LTST) and 13:00 LTST for (a) all six MY of the Mars Science Laboratory mission, (b) Phoenix, and (c) Pathfinder. Duration refers to the half-period of the correlated cosine in minutes. The amplitude is calculated by squaring the average across each period for every hour of correlation.

Rapid increases in dust optical depth associated with passing dust storms at the end of the mission were observed to correspond to condensate clouds and increased dust devil activity (Ellehoj et al., 2010), suggesting the likely passage of weather systems. In particular, events on sols 128 ($L_s = 136^\circ$) and sol 150 ($L_s = 147^\circ$) are evident in the results of Figure 8b as decreases in variance. This is discussed in more detail in Section 5.2.

Not as evident but still visible in the temperature data (see Figure 4b) is a small and consistent increase in variance near 22:00 LTST. Whereas increases in nighttime turbulence were likely associated with forced convection for the MER missions (Mason & Smith, 2021), the increases here could be a response to latent heat release (Holstein-Rathlou et al., 2010; Zent et al., 2016).

The seasonal signature is less evident for Pathfinder (Figure 8c). This mission was shorter (84 sols) than the Phoenix mission (151 sols), and measurement periods were limited. There was an increase later in the season, corresponding to northern fall and the equinox. While this pattern is similar to that of Phoenix temperature, it is also worth noting that measurement periods toward the end of the mission increased in length from minutes to hours. It is possible that the limited length of time at the beginning of the mission was not long enough to capture the largest changes in variance occurring on the order of minutes.

4.2. Duration of Structures

The structures present within the temperature data set are assessed using cosine correlation calculations as discussed in Section 3.3. Each panel in Figure 9 contains results for the correlation coefficient plotted as a function of mission sol and displayed below the actual fluctuations for the noontime hour. This hour begins at 12:00 LTST. The correlations are calculated only for extended blocks, which is why Pathfinder results in Figure 9c are sparsely populated. We chose the noontime hour for comparison despite the peak of fluctuations occurring closer to 14:00 LTST for MSL because the noontime hour is consistently covered in the REMS observations.

There is a positive correlation between larger temperature fluctuations and correlation periods. This is expected, as larger eddy structures in the temperature signature should have stronger intensity and duration when passing over the temperature sensors. This is evident in Figure 9b for the Phoenix mission, which shows a drop in fluctuation magnitude as well as structure duration toward the end of the mission. In addition, the temperature signal shows smaller structures at the beginning of the mission, when variance peaks early and is suppressed in the

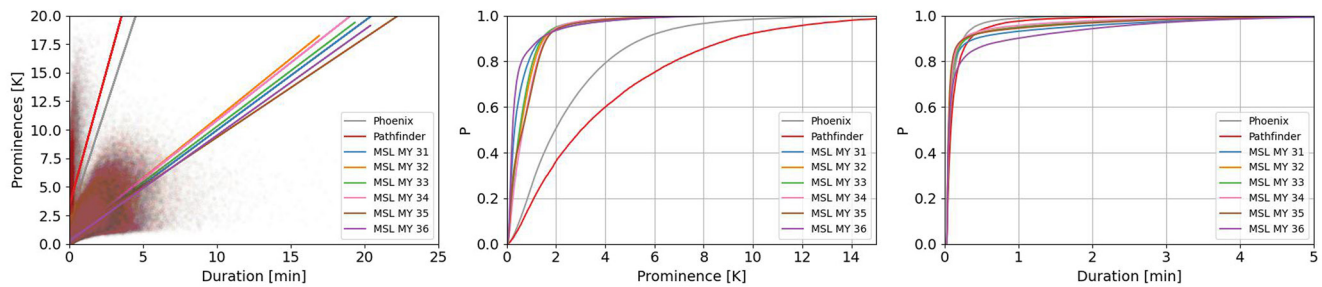


Figure 10. (Left panel) Prominences versus durations for each mission (middle panel) cumulative distribution of prominences for each mission, and (right panel) cumulative distribution of durations for each mission.

afternoon. For MSL, this pattern emerges in Figure 9a, where fluctuations near sol 1100 (MY 33, $L_s \sim 50^\circ$) correspond to shorter periods, and periods during the global dust storm near sol 2100 (MY 34, $L_s \sim 180^\circ$) tend to also be shorter. MSL tends to have larger period structures, showing higher correlations near 2 and 4 min for MY 34 and 32. Phoenix and Pathfinder correlations tend to peak below 2 min. Fluctuations with periodic signatures tend to occur near $L_s = 270^\circ$ in the detrended MSL data for all MY except MY 34 when observations were not taken.

There is a lack of short-period signatures in the MSL data, despite the lower variance. This is expected due to the slower time constant. Correspondence of variance and period length is not one for one for all three missions. To assess this, we can analyze the signal in a different way, as shown in Figure 10. For each hour on each sol (and for each mission), we can look at only the peaks in temperature as opposed to the correlations in temperature. The difference is that correlations can be negative, whereas finding the peaks ignores the troughs or instances of assumed downwelling subsidence. For every local peak in the temperature signal, the duration is determined using the value at the base of the peak prominence relative to the maximum value within the peak. Here, the differences in magnitude between MSL, Phoenix and Pathfinder are evident, but the durations are still comparable. There is no discernible trend in MY for MSL.

5. Discussion

Overall, there are clear seasonal and diurnal trends in the variance of temperature for the three missions. We are interested not only in how the temperature behaves seasonally and diurnally but also in what might potentially drive these behaviors. Variability can be caused by forced or free convection. These types of convection occur through changes in local and regional circulation and local shear development or through the generation of warm thermals rising from the surface. The response of air temperature variation at the surface is controlled by many factors, including weather systems, surface properties, latitude, and topography. These factors can be present in the air temperature data and therefore make the analysis complex. We discuss the potential drivers as they pertain to each mission in the next section.

5.1. Interannual Variability of MSL REMS

Figures 11 and 12 show the seasonal and diurnal magnitudes of air temperature variance, respectively, averaged over either 30 sols (diurnal, Figure 12) or several hours (seasonal, Figure 11). Each MY for MSL is distinguished in the left panels of Figure 11 and is compared to Pathfinder and Phoenix in the right panels. Averages are indicated with plus markers, and a smoothing filter with a window of 21 sols is applied to the seasonal results in Figure 11. In Figure 12, averages are reported for each hour without smoothing.

The lower variances for MSL when compared to Phoenix and Pathfinder are more noticeable when comparing the left and right panels of Figure 11. Both Pathfinder and Phoenix exhibit increases over their respective missions with a tailing drop toward the end. For Pathfinder, this is likely due to the limited observation periods at the beginning of the mission. Pathfinder observed the atmosphere just after the northern summer solstice (defined at $L_s = 90^\circ$), and both insolation and optical depth did not change drastically during that time (e.g., Martínez et al., 2017).

At the Phoenix location, the decrease in temperature variance at the end of the mission was related to the onset of northern fall and longer nights. This is accompanied by a drop in longer-period structures (Figure 9b). Insolation

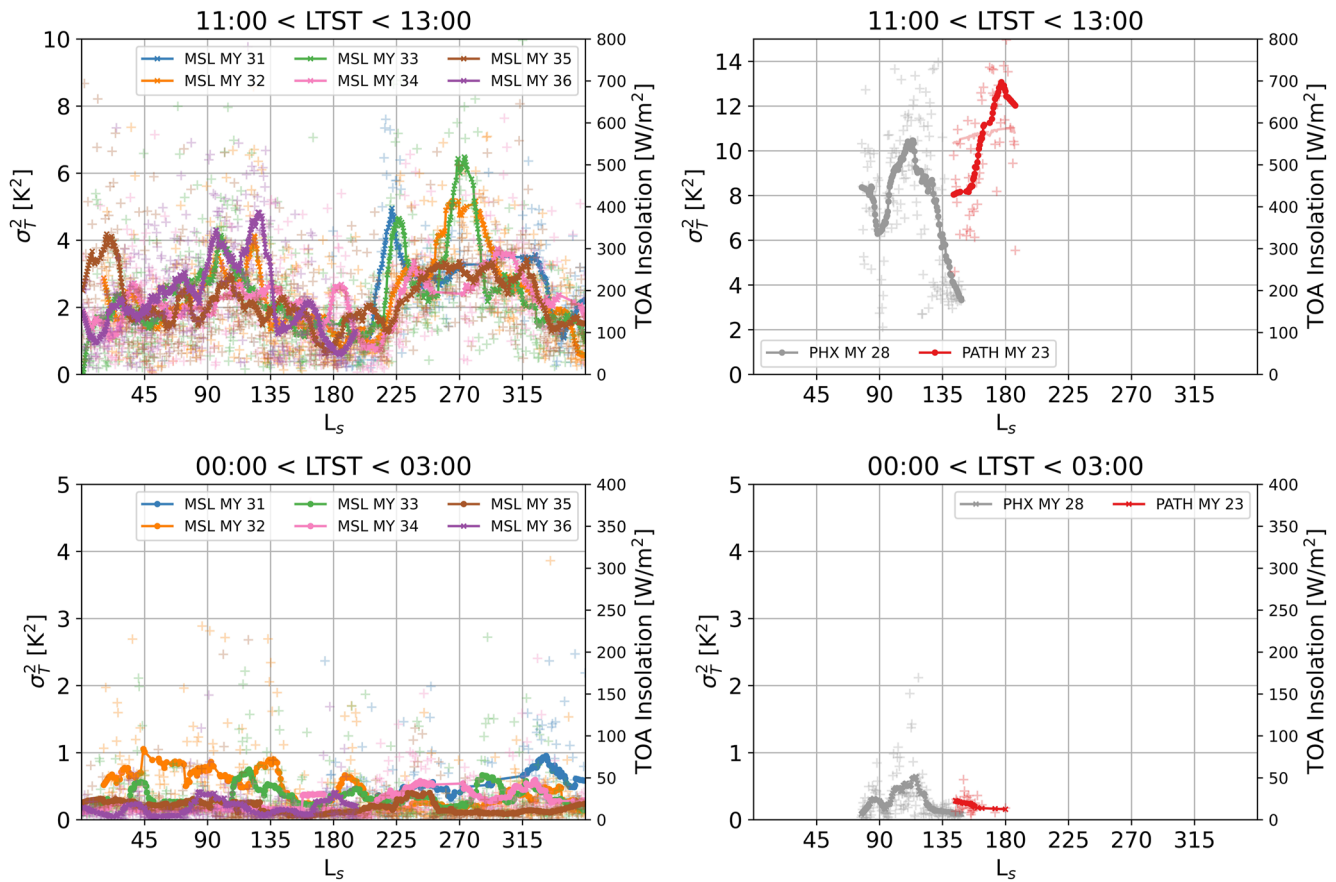


Figure 11. Seasonal variation in afternoon (top panels) and midnight hours (bottom panels) for Mars Science Laboratory (left panels) compared with Pathfinder and Phoenix (right panels). The hourly averages shown in Figure 8 are indicated here with plus markers and smoothed over 21 sols.

dropped quickly after sol 80 of the mission and both fog and precipitation were observed (Whiteway et al., 2008). As a result of the reduced insolation, convection was weaker at that time. For the morning hours, both Phoenix and Pathfinder fall below the assumed noise range. There is an increase in activity for Phoenix and Pathfinder during the hours just after sunset (Schofield et al., 1997; Zent et al., 2016), but the fluctuations are much smaller than those during the day.

The MSL seasonal pattern exhibits maxima near $L_s \sim 90^\circ$ and $L_s \sim 270^\circ$. The local maximum near $L_s = 90^\circ$ is less prominent and is noisier, having values mostly ranging from 0 to 5 K², while the peak at $L_s = 270^\circ$ ranges

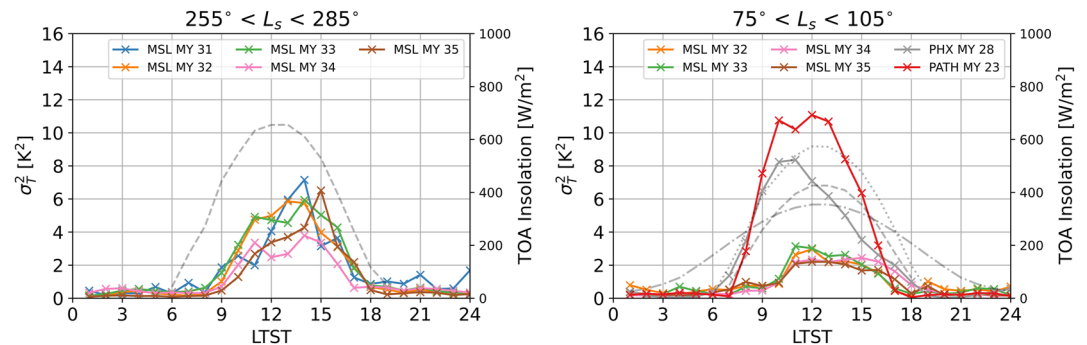


Figure 12. Diurnal comparisons over 30 sols for timeframes falling near southern hemispheric summer (left) and southern hemispheric winter (right) for all missions. Gray lines represent hourly averaged insolation. The dashed gray lines correspond to hourly averaged insolation at the latitude of the Mars Science Laboratory (MSL) mission. The dotted, dashed, dash-dotted lines correspond to hourly-averaged insolation at Pathfinder, MSL, and Phoenix, respectively.

from about 1 to 7 K². Visible within Figure 11 is the difference between MY 34 and MY 35 compared to the other MY's. The peaks at $L_s \sim 270^\circ$ are muted or capped during these two years compared to the previous two years. MY 31 lacks observations during this time, and so also appears muted. However, we would expect the observations during this period to mimic those of MY 32 and MY 33. In addition, the decrease in variance during the onset of the global dust storm at Gale crater in MY 34 is preceded by a very small increase just before. It is apparent from the MSL temperature variance results that high optical depth corresponds to lowered variance when the optical depth is associated with dust storms (see Figures 14b and 14c, shaded gray regions for examples of the seasonal timing). This is due to the overall homogenization of the vertical temperature profile and the reduction in the surface to air temperature gradient. However, there is some discussion as to whether turbulent activity increases at the onset of a dust storm, and whether dust has some positive feedback on thermal convection (Spiga, 2021; Wu et al., 2021). In addition, Zurita-Zurita et al. (2022) found that specific surface pressure oscillations in Gale crater preceded increases in dust opacity, some of which coincided prior to the MY 34 global dust storm. Figure 11, top left panel shows a small increase in variance just before the onset of the global dust storm in MY 34, $L_s \sim 180^\circ$. This is notable because a global minimum tends to exist here in all other years. However, the overall magnitude of this increase is small and is not noticeable before other regional or local dust storms. For instance, variance in MY 36, $L_s \sim 150^\circ$ is like the patterns in temperature variance of previous MY's, and any increases are hidden within this seasonal pattern.

Morning hours for MSL do not exhibit strong variability above the adopted noise level, but early MY 32 and late MY 31 do show increases in activity that are not present in the other MY. This could be due to the nature of noise, as this is not only a very cold time of the year but also within the crater basin. If a minimum wind speed is necessary to obtain an accurate temperature measurement, then a lack of wind speed would cause greater noise. This would imply that wind speeds at higher elevations are larger, which is consistent with a decrease in early morning temperature fluctuations as the rover traverses Mount Sharp.

Figure 12 shows diurnal patterns for each MY of the MSL mission at $L_s = 270^\circ$ averaged over 30 sols compared to that of Phoenix and Pathfinder at $L_s = 90^\circ$ averaged over 30 sols. Light gray dashed and dotted lines representing average hourly solar irradiance for each mission are shown in the figure for reference. These correspond to Top of Atmosphere modeled values. The peak of the diurnal signal for Pathfinder (red) and Phoenix (dark gray) trends toward morning and at noon hours, while those of MSL peak later near 15:00 LTST. Both Phoenix and Pathfinder environments become strongly variable just after 6:00 LTST and have a distinct quiet period near 17:00 LTST, as observed in other missions (Chatain et al., 2021; Mason & Smith, 2021). During this same season in Gale crater, variance does not increase until roughly 09:00 LTST. During the southern hemispheric winter season, this onset is much later. The sensor height of REMS is roughly at 1.6 m, which is higher than that of the Pathfinder at 1.1 m. As the height above the surface increases, the temperature variance should decrease. However, the Phoenix top of the mast sensor was located 2 m above the ground. The shift to early morning hours is weighted by the beginning and end of mission variance profiles, which are dominated by afternoon decreases in variance.

5.2. Drivers of Temperature Response

5.2.1. Solar Irradiance and Dust Loading

Diurnal atmospheric temperature evolution near the surface depends on the balance between downwelling and upwelling energy. On Mars, the incoming radiative forcing plays a larger role than other forcings (Haberle et al., 2017; Martínez et al., 2023). The atmosphere tends to be transparent to visible wavelengths at the peak of solar emission. The surface reflects some of the incoming shortwave radiation and absorbs the rest. This incoming solar radiation, along with the thermal inertia and albedo of the surface, determines the available energy that is then emitted upward into the atmosphere (e.g., Stull, 1988). Eddies and thermals form as a response to this surface emission. Changes in the seasonal insolation should correspond to seasonal changes in the temperature variance. This is true to some extent for all three missions. For instance, insolation is greatest at the MSL location near the perihelion during southern summer, while insolation is largest for Pathfinder and Phoenix during northern summer. Both Pathfinder and Phoenix operated during the peak of insolation, meaning that the temperature fluctuations were likely at a maximum for each location. This is evident in the decrease in temperature variance for Phoenix at the end of its mission lifetime.

Atmospheric optical depth affects the incoming sunlight by reducing the radiation received at the surface. It is only at relatively high optical depth values that the extinction is significant enough to offset any other effects. During the Phoenix mission, higher optical depth was reported at the beginning and end of the mission, which

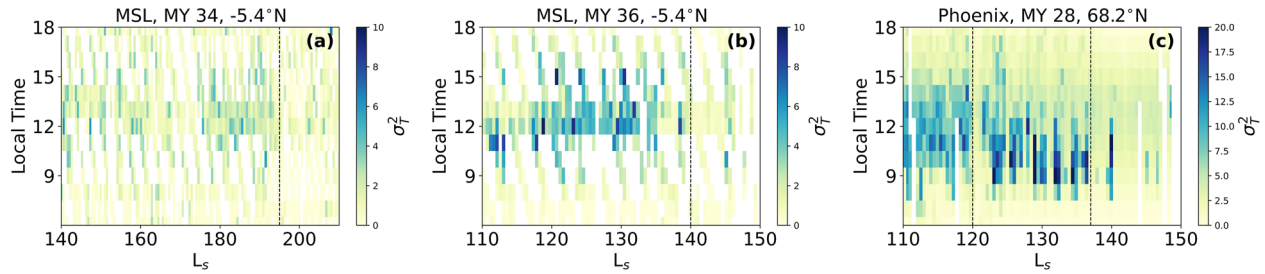


Figure 13. Panels (a, b) show selected locations of variance from Figure 8 and highlight known locations of dust storm activity for Mars Science Laboratory using the dashed gray lines. Similarly, the end of the Phoenix mission shows similar decreases in variance during times when likely frontal dust activity was occurring (Holstein-Rathlou et al., 2010).

was consistent with the frontal dust storm activity. At the beginning of the mission, the sustained high optical depth was attributed to non-local dust lifting (Holstein-Rathlou et al., 2010) that added to the overall background of dust. During the middle of the mission, when the optical depth was lower and insolation was at its peak, noontime variance increased over those sols. Evidence of frontal activity was observed over the Phoenix mission between $L_s = 110^\circ$ and $L_s = 140^\circ$. One such event at $L_s = 120^\circ$, marked in Figure 13c with a dotted gray line, was followed by a period of decreased temperature fluctuations of 2 K. This decrease of 2–3 K is also seen in the MSL temperature fluctuation results for MY 34, $L_s = 195^\circ$ (Figure 13a, dotted gray line and Figure 14) and MY 36, $L_s = 140^\circ$ (Figure 13b, dotted gray line, and Figure 14). While the former results in a strong decrease in variance across all hours, the latter shows a much smaller decrease in line with seasonal changes. However, the decrease is still evident.

While Phoenix and Pathfinder strongly follow seasonal variations in solar insolation, MSL temperature variations show a double peaked structure, one near each solstice. The local maximum at $L_s = 90^\circ$ could be driven

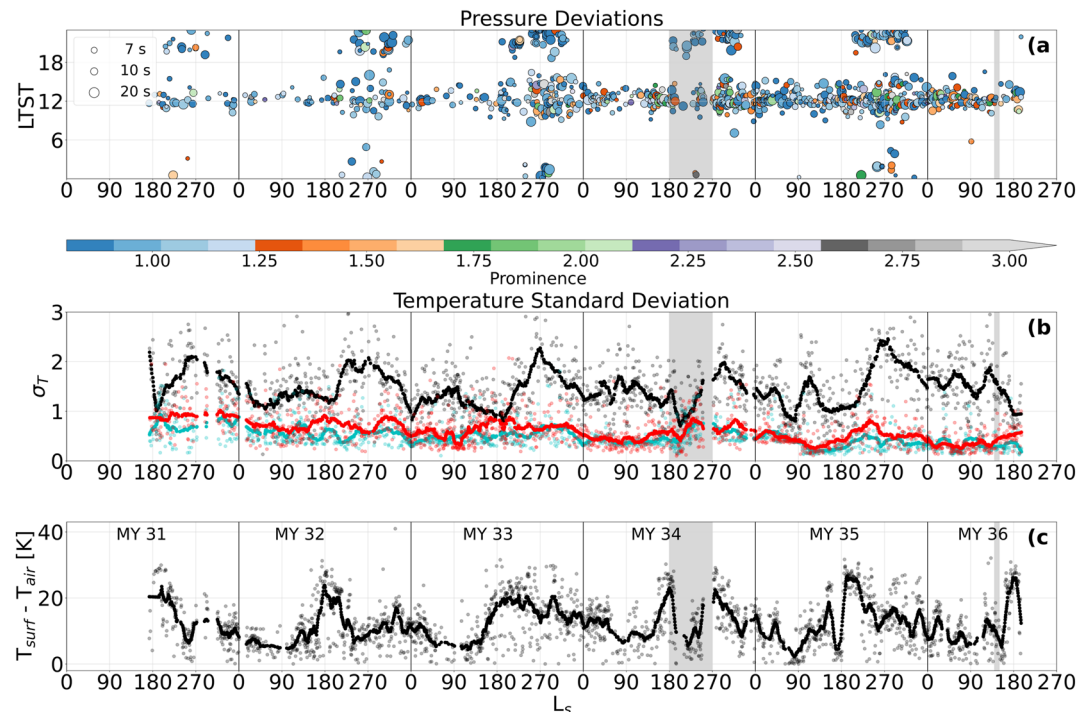


Figure 14. Panel (a) shows unfiltered drops in the detrended pressure data. This is compared to noon time standard deviation in air temperature in panel (b) and noontime surface to air temperature difference in panel (c). Colors in panel (a) represent the magnitude of the pressure drops, and sizes represent the Full Width at Half Maximum durations. Dark shaded regions represent major increases in dust optical depth associated with dust storm activity. The light blue and red lines in panel (b) show morning (03:00 local true solar time [LTST]) and evening (20:00 LTST) temperature variances.

by illumination of the local slope during the daytime while the subsolar point is in the northern hemisphere. MSL sits on the northern slope of Mount Sharp, and therefore saw more direct sunlight during this time of year. However, this is also a time of year when the return flow of the Hadley cell is moving from south to north. Winds are stronger during this time (Fonseca et al., 2018), and air temperatures are much lower (see Figure 1). There are several reasons the double peak could exist, ranging from cold-temperature noise to dynamics to radiation on the northern-facing slopes. In addition, daily maximum irradiance at the MSL location also shows two annual peaks (Martínez et al., 2021). While it is convenient to say that the cause is simply increased noise, the noise limit shown in Figure 5b suggests that the variance at noon falls above the noise limit; it is possible that some real atmospheric phenomenon could be occurring at this point. We save a detailed analysis of this for future work.

5.2.2. Surface Properties, Mechanical Generation, and Pressure

While solar radiation and atmospheric optical depth dictate the amount of radiation reaching the surface, the properties of the underlying soil dictate how much heat the surface retains, which then in turn dictates how the surface warms the atmosphere from below. Thermal inertia is one of the properties that controls this heating. High thermal inertia means that a surface will take a long time to heat up or cool down. It has a large capacity to absorb heat. It also tends to emit for longer periods of time. Lower thermal inertia, like that at Phoenix, causes surfaces to respond quickly to temperature changes, and these surfaces tend to cool or heat quickly. All three locations vary in their terrain and surface properties (Bell, 2008; Putzig & Mellon, 2007). In addition, each location experiences different air flows and circulations, which drive and redistribute air in seasonal and diurnal patterns.

On average, thermal inertia at MSL and Pathfinder (greater than $386 \text{ J m}^{-2} \text{ K}^{-1} \text{ s}^{-1/2}$) Putzig and Mellon (2007) are similarly higher than those at the Phoenix location (near $200 \text{ J m}^{-2} \text{ K}^{-1} \text{ s}^{-1/2}$) (Bandfield, 2007). This suggests that even though Phoenix is at a higher latitude, it should have a larger surface response in variability. This is seen in the temperature variability data when compared to that of Pathfinder. Both have similar magnitudes in variance despite differences in solar forcing. While MSL and Pathfinder fall in similar thermal inertia regions, MSL, even when looking at the modeled temperatures, does not exhibit significantly larger variability than Pathfinder despite its near-equatorial location.

We compare the MSL REMS temperature standard deviation to the difference in surface and air temperature. The temperature difference between the air and the surface drives free convection and is related to the lapse rate of the atmosphere as well as the thermal inertia of the surface. In addition, we compare seasonal changes in noontime variance with pressure drops larger than 0.6 Pa identified in the pressure data. We compare the temperature variance to surface-to-air temperature difference and pressure deviations or drops for MSL data in Figures 14c and 14a, respectively. Gaps in the observation are shown in Figures 14b and 14c.

With enough vorticity introduced into the system, convective vortices can form at the boundaries between thermal sheets. These vortices which are indicated in the pressure signal through pressure drops (Kahanpää et al., 2016; Martínez et al., 2021; Newman et al., 2019; Ordoñez-Etxeberria et al., 2020). Pressure drops associated with convective vortex activity are also indicators of atmospheric surface layer activity. Seasonal and diurnal patterns in the vortex activity serve to help verify the atmospheric component of temperature variations shown in this work. In this work, we do not present an exhaustive analysis of convective vortices in Gale Crater, as this has been done before for previous work (e.g., Newman et al., 2019; Ordoñez-Etxeberria et al., 2020). Instead, we detrend the pressure data using the same running mean and search for pressure drops with a change in the detrended pressure greater than 0.6 Pa. We calculate both the maximum depth relative to the surrounding curve and a duration at half the maximum depth for each one (Full Width at Half Maximum). These are presented in Figure 14a as color and size, respectively. We do not filter for double-peaked structures and structures that may be more indicative of convection rather than vortices, which is a task saved for future work. Despite the simplistic approach, the results of our search are consistent with previous work for the site (e.g., Guzewich et al., 2019; Ordoñez-Etxeberria et al., 2020), showing an increase in the number of vortices detected as the rover traversed Mt. Sharp (see Figure 2 for changes in elevation). Since the temperature variance calculated from local boom 1 ATS measurements does not increase or decrease, this could be due to shear from increasing wind speeds. This would also explain the noisier nighttime results for temperature variance for the first 2 years, which decreases with increasing elevation (See Figure 14b). Where thermal contrast of the sensors is necessary to reduce noise and collect data, the reduction in variance at night as the rover traverses might suggest that the wind speed is increasing.

The noontime surface to air temperature difference is shown in Figure 14c. The seasonal pattern is much more variable due to the changing terrain as the rover traverses along its route. However, there is a general single-peak

pattern showing increased differences during southern hemispheric summer and a decrease during southern hemispheric winter. The magnitude of this difference is consistent from year to year, which could explain why the temperature variance is so consistent in magnitude. There are some points where the variance in noontime temperature does not correspond to that of the surface-to-air temperature difference, including MY 32, $L_s = 180^\circ$, indicating the complexity of processes occurring at this location. In general, however, the variance tends to follow the surface-to-air temperature difference, and therefore the lapse rate, which is in turn dictated by the strength of the incoming solar radiation and the properties of the surface.

6. Conclusions

We compare temperature data sets from three missions: MSL, Phoenix, and Pathfinder. These data sets contain information about atmospheric surface layer responses to forcing. To understand this behavior, we detrend the data sets, retaining only fluctuations in air temperature on the scales of seconds to minutes. These are compared seasonally, diurnally, and to other meteorological measurements. We compare these measurements statistically through variance as a proxy for daytime convective intensity and look at changes in frequency patterns through correlation plots.

MSL REMS air temperature, which contains more than five MY of measurements, shows a consistent year-to-year seasonal pattern, with increased temperature variance in southern summer and a secondary, smaller local maximum near southern winter in aphelion. These peaks correspond to the two solstice periods when winds are strongest in and around the crater (Rafkin et al., 2016).

Phoenix and Pathfinder temperature variances follow patterns of insolation, with moderate afternoon decreases during times of higher optical depth. The diurnal temperature variance peaks closer to noon for Pathfinder and before noon for Phoenix. This morning peak is consistent with frontal dust storm activity during the afternoon hours later in the mission, which reduces incoming solar radiation and therefore the response of the atmosphere to decreased warming from the surface.

Magnitudes of temperature variance are higher for Phoenix and Pathfinder than for MSL. Pathfinder air temperature variance is the highest of the three, despite its higher thermal inertia, which acts as a barrier for heat transfer to the atmosphere. This is likely due to both Pathfinder being at a lower latitude than that of Phoenix and at a site with lower albedo. Latitude tends to govern climates more so than anything else because it dictates the amount of solar radiation reaching the ground, but the lower variances at MSL, even in the modeled temperature data, point to influences from local crater flows, which would act to redistribute energy, and suppress the boundary layer within the crater (Rafkin et al., 2016). Modeling of local crater dynamics can help validate the overall influence of crater boundary layer suppression, and we leave this task for future work.

The number of drops greater than 0.6 Pa calculated using detrended observations of pressure shows an increased frequency of occurrence with elevation, while the noontime temperature variance remains constant. Noontime differences in the surface-to-air temperatures also remain constant from year to year, showing that temperature variance likely follows more closely the response to surface conditions, while pressure drops are influenced both by the surface-to-air temperature difference and by the local dynamics and availability of shear. This is consistent with results from Earth field observations recording dust devil activity in the Atacama Desert in South America, which links dust devil origination to local meteorology and the vertical distribution of temperature and wind (Kurgansky et al., 2011). Local winds within the Gale crater likely play a significant role in the dust devil formation. During the global dust storm in MY 34 near $L_s \sim 180^\circ$, both the number of pressure drops and the amplitude of the temperature variance decreased, consistent with a decrease in the surface-to-air temperature difference and less solar irradiance reaching the surface.

This work demonstrates how atmospheric variance responds to local conditions, and how its study can be enhanced through intermission and inter-instrument comparisons, as different instruments and sites provide insight into different atmospheric phenomena.

Data Availability Statement

All air temperature and pressure data are available on the Planetary Data System Planetary Atmospheres Node for all three missions. Phoenix temperature data are available in meteorology (MET) package files on the PDS (Dickinson, 2008). Pathfinder air temperature data are also contained within a meteorological data

package (Murphy, 1999) on the PDS. Mars Science Laboratory data were collected from two distinct sets. Air temperatures are taken from the ENVRDR data records (Gómez-Elvira, 2013b), while pressures are taken from the MODRDR data records (Gómez-Elvira, 2013c). Ancillary information is calculated using spice kernels produced from the Navigation and Ancillary Information Facility (Acton, 1996) and from MSL REMS ADR files (Gómez-Elvira, 2013a).

In addition, the data produced in this work have been uploaded to a Mendeley repository, including temperature variance files for MSL, Phoenix, and Pathfinder calculated using detrended data and correlation data using temperature around solar noon. All are available on the Mendeley repository at (Mason, 2023).

Acknowledgments

The material is based upon work supported by NASA under Award 80GSFC21M0002 and is funded through the NASA ROSES Mars Data Analysis Program, NNN20ZDA001N-MDAP. Guzewich is supported by the Mars Science Laboratory Participating Scientist program.

References

- Acton, C. H. (1996). Ancillary data services of NASA's navigation and ancillary information facility. *Planetary and Space Science*, 44(1), 65–70. [https://doi.org/10.1016/0032-0633\(95\)00107-7](https://doi.org/10.1016/0032-0633(95)00107-7)
- Bandfield, J. L. (2007). High-resolution subsurface water-ice distributions on Mars. *Nature*, 447(7140), 64–67. <https://doi.org/10.1038/nature05781>
- Banfield, D., Spiga, A., Newman, C., Forget, F., Lemmon, M., Lorenz, R., et al. (2020). The atmosphere of Mars as observed by InSight. *Nature Geoscience*, 13(3), 190–198. <https://doi.org/10.1038/s41561-020-0534-0>
- Bell, J. (2008). *The Martian surface: Composition, mineralogy and physical properties*. Cambridge University Press.
- Chamberlain, T. E., Cole, H. L., Dutton, R. G., Greene, G. C., & Tillman, J. E. (1976). Atmospheric measurements on Mars: The Viking meteorology experiment. *Bulletin of the American Meteorological Society*, 57(9), 1094–1104. [https://doi.org/10.1175/1520-0477\(1976\)057<1094:amomtv>2.0.co;2](https://doi.org/10.1175/1520-0477(1976)057<1094:amomtv>2.0.co;2)
- Chatain, A., Spiga, A., Banfield, D., Forget, F., & Murdoch, N. (2021). Seasonal variability of the daytime and nighttime atmospheric turbulence experienced by InSight on Mars. *Geophysical Research Letters*, 48(22), e2021GL095453. <https://doi.org/10.1029/2021GL095453>
- Christensen, J. R., Arvidson, R. E., O'Sullivan, J. A., Vasavada, A. R., & Weitz, C. M. (2022). CRISM-based high spatial resolution thermal inertia mapping along curiosity's traverse in Gale Crater. *Journal of Geophysical Research: Planets*, 127, e2021JE007076. <https://doi.org/10.1029/2021JE007076>
- Davy, R., Davis, J. A., Taylor, P. A., Lange, C. F., Weng, W., Whiteway, J., & Haraldur Gunnlaugson, P. (2010). Initial analysis of air temperature and related data from the Phoenix MET station and their use in estimating turbulent heat fluxes. *Journal of Geophysical Research*, 115(E3), E00E13. <https://doi.org/10.1029/2009JE003444>
- Dickinson, C. D. (2008). PHX METEOROLOGICAL DATA V1.0. NASA Planetary Data System. <https://doi.org/10.17189/11t5-kp51>
- Edgett, K. S., & Christensen, P. R. (1997). Rocks and aeolian features in the Mars Pathfinder landing site region: Viking infrared thermal mapper observations. *Journal of Geophysical Research*, 102(E2), 4107–4116. <https://doi.org/10.1029/96JE02825>
- Ellehoj, M. D., Gunnlaugsson, H. P., Taylor, P. A., Kahanpää, H., Bean, K. M., Cantor, B. A., et al. (2010). Convective vortices and dust devils at the Phoenix Mars mission landing site. *Journal of Geophysical Research*, 115(E4), E00E16. <https://doi.org/10.1029/2009JE003413>
- Farley, K. A., Williford, K. H., Stack, K. M., Bhartia, R., Chen, A., de la Torre, M., et al. (2020). Mars 2020 mission overview. *Space Science Reviews*, 216(8), 142. <https://doi.org/10.1007/s11214-020-00762-y>
- Fonseca, R. M., Zorzano-Mier, M.-P., & Martín-Torres, J. (2018). Planetary boundary layer and circulation dynamics at Gale Crater, Mars. *Icarus*, 302, 537–559. <https://doi.org/10.1016/j.icarus.2017.11.036>
- Gómez-Elvira, J. (2013a). Mars Science Laboratory rover environmental monitoring station RDR data V1.0, MSL-M-REMS-6-ADR-V1.0. NASA Planetary Data System. <https://doi.org/10.17189/1523030>
- Gómez-Elvira, J. (2013b). Mars Science Laboratory rover environmental monitoring station RDR data V1.0, MSL-M-REMS-4-ENVRDR-v1.0. NASA Planetary Data System. <https://doi.org/10.17189/23015>
- Gómez-Elvira, J. (2013c). Mars Science Laboratory rover environmental monitoring station RDR data V1.0, MSL-M-REMS-4-MODRDR-v1.0. NASA Planetary Data System. <https://doi.org/10.17189/23015>
- Gómez-Elvira, J., Armiens, C., Carrasco, I., Genzer, M., Gómez, F., Haberle, R., et al. (2014). Curiosity's rover environmental monitoring station: Overview of the first 100 sols. *Journal of Geophysical Research: Planets*, 119(7), 1680–1688. <https://doi.org/10.1002/2013JE004576>
- Gómez-Elvira, J., Armiens, C., Castañer, L., Domínguez, M., Genzer, M., Gómez, F., et al. (2012). REMS: The environmental sensor suite for the Mars Science Laboratory rover. *Space Science Reviews*, 170(1–4), 583–640. <https://doi.org/10.1007/s11214-012-9921-1>
- Grotzinger, J. P., Crisp, J., Vasavada, A. R., Anderson, R. C., Baker, C. J., Barry, R., et al. (2012). Mars Science Laboratory mission and science investigation. *Space Science Reviews*, 170(1–4), 5–56. <https://doi.org/10.1007/s11214-012-9892-2>
- Guzewich, S. D., de la Torre Juárez, M., Newman, C. E., Mason, E., Smith, M. D., Miller, N., et al. (2021). Gravity wave observations by the Mars Science Laboratory REMS pressure sensor and comparison with mesoscale atmospheric modeling with MarsWRF. *Journal of Geophysical Research: Planets*, 126, 8. <https://doi.org/10.1029/2021JE006907>
- Guzewich, S. D., Lemmon, M., Smith, C. L., Martínez, G., De Vicente-Retortillo, Á., Newman, C. E., et al. (2019). Mars Science Laboratory observations of the 2018/Mars Year 34 global dust storm. *Geophysical Research Letters*, 46(1), 71–79. <https://doi.org/10.1029/2018GL080839>
- Haberle, R. M., Todd, C. R., François, F., Smith, M. D., & Zurek, R. W. (2017). *The atmosphere and climate of Mars*. Cambridge Planetary Science, Cambridge University Press. <https://doi.org/10.1017/9781139060172>
- Holstein-Rathlou, C., Gunnlaugsson, H. P., Merrison, J. P., Bean, K. M., Cantor, B. A., Davis, J. A., et al. (2010). Winds at the Phoenix landing site. *Journal of Geophysical Research*, 115(E5), E0018. <https://doi.org/10.1029/2009JE003411>
- Kahanpää, H., Newman, C., Moores, J., Zorzano, M.-P., Martín-Torres, J., Navarro, S., et al. (2016). Convective vortices and dust devils at the MSL landing site: Annual variability. *Journal of Geophysical Research: Planets*, 121(8), 1514–1549. <https://doi.org/10.1002/2016JE005027>
- Kurgansky, M. V., Montecinos, A., Villagran, V., & Metzger, S. M. (2011). Micrometeorological conditions for dust-devil occurrence in the Atacama Desert. *Boundary-Layer Meteorology*, 138(2), 285–298. <https://doi.org/10.1007/s10546-010-9549-1>
- Martínez, G. M., De Vicente-Retortillo, A., Vasavada, C. E., Newman, C. E., Fischer, E., Rennó, N. O., et al. (2021). The surface energy budget at Gale Crater during the first 2500 sols of the Mars Science Laboratory mission. *Journal of Geophysical Research: Planets*, 126(9), e2020JE006804. <https://doi.org/10.1029/2020JE006804>
- Martínez, G. M., Newman, C. N., De Vicente-Retortillo, A., Fischer, E., Renno, N. O., Richardson, M. I., et al. (2017). The modern near-surface Martian climate: A review of in-situ meteorological data from Viking to Curiosity. *Space Science Reviews*, 212(1–2), 295–338. <https://doi.org/10.1007/s11214-017-0360-x>

- Martínez, G. M., Sebastián, E., Vicente-Retortillo, A., Smith, M. D., Johnson, J. R., Fischer, E., et al. (2023). Surface energy budget, albedo, and thermal inertia at Jezero Crater, Mars, as observed from the Mars 2020 MEDA instrument. *Journal of Geophysical Research: Planets*, 128(2), e2022JE007537. <https://doi.org/10.1029/2022JE007537>
- Mason, E. L. (2023). Processed temperature variances for Mars Science Laboratory, Phoenix, and Pathfinder. *Mendeley Data*, V2. <https://doi.org/10.17632/m34hh5gbfm.2>
- Mason, E. L., & Smith, M. D. (2021). Temperature fluctuations and boundary layer turbulence as seen by Mars Exploration rovers miniature thermal emission spectrometer. *Icarus*, 360, 114350. <https://doi.org/10.1016/j.icarus.2021.114350>
- Miller, N. M., de la Torre Juárez, M., & Tampari, L. (2018). The effect of Bagnold dunes slopes on the short timescale air temperature fluctuations at Gale Crater on Mars. *Geophysical Research Letters*, 45(21), 11588–11594. <https://doi.org/10.1029/2018GL080542>
- Munguira, A., Hueso, R., Sánchez-Lavega, A., de la Torre-Juarez, M., Martínez, G. M., Newman, C. E., et al. (2023). Near surface atmospheric temperatures at Jezero from Mars 2020 MEDA measurements. *Journal of Geophysical Research: Planets*, 128(3), e2022JE007559. <https://doi.org/10.1029/2022JE007559>
- Murphy, J. R. (1999). MPFL Mars ATM STRUCT INST/MET PKG 3 RDR surface v1.0, MPFL-M-ASIMET-3-RDR-SURF-V1.0. *NASA Planetary Data System*, 1009. <https://doi.org/10.17189/nh81-cg55>
- Newman, C. E., Kahanpää, H., Richardson, M. I., Martínez, G. M., Vicente-Retortillo, A., & Lemmon, M. T. (2019). Convective vortex and dust devil predictions for gale crater over 3 Mars Years and comparison with MSL-REMS observations. *Journal of Geophysical Research: Planets*, 124(12), 3442–3468. <https://doi.org/10.1029/2019JE006082>
- Ordóñez-Etxeberria, I., Hueso, R., & Sánchez-Lavega, A. (2020). Strong increase in dust devil activity at Gale Crater on the third year of the MSL mission and suppression during the 2018 Global dust storm. *Icarus*, 347, 113814. <https://doi.org/10.1016/j.icarus.2020.113814>
- Putzig, N. E., & Mellon, M. T. (2007). Apparent thermal inertia and the surface heterogeneity of Mars. *Icarus*, 191(1), 68–94. <https://doi.org/10.1016/j.icarus.2007.05.013>
- Rafkin, S. C. R., Pla-García, J., Kahre, M., Gomez-Elvira, J., Hamilton, V., Marín, M., et al. (2016). The meteorology of Gale Crater as determined from rover environmental monitoring station observations and numerical modeling. Part II: Interpretation. *Icarus*, 280, 114–138. <https://doi.org/10.1016/j.icarus.2016.01.031>
- Read, P., Galperin, B., Larsen, S., Lewis, S., Määttä, A., Petrosyan, A., et al. (2017). The Martian planetary boundary layer. In R. Haberle, R. Clancy, F. Forget, M. Smith, & R. Zurek (Eds.), *The atmosphere and climate of Mars (Cambridge Planetary Science)* (pp. 172–202). Cambridge University Press. <https://doi.org/10.1017/9781139060172.007>
- Rodriguez-Manfredi, J. A., de la Torre Juárez, M., Sanchez-Lavega, A., Hueso, R., Martínez, G., Lemmon, M. T., et al. (2023). The diverse meteorology of Jezero Crater over the first 250 sols of perseverance on Mars. *Nature Geoscience*, 16(1), 19–28. <https://doi.org/10.1038/s41561-022-01084-0>
- Ryan, J. A., & Henry, R. M. (1979). Mars atmospheric phenomena during major dust storms, as measured at the surface. *Journal of Geophysical Research*, 84(B6), 2821–2829. <https://doi.org/10.1029/JB084iB06p02821>
- Schofield, J. T., Barnes, J. R., Crisp, D., Haberle, R. M., Larsen, S., Magalhães, J. A., et al. (1997). The Mars Pathfinder Atmospheric Structure Investigation/Meteorology (ASI/MET) experiment. *Science*, 278, 5344. <https://doi.org/10.1126/science.278.5344.1752>
- Seiff, A., Tillman, J. E., Murphy, J. R., Schofield, J. T., Crisp, D., Barnes, J. R., et al. (1997). The atmosphere structure and meteorology instrument on the Mars Pathfinder lander. *Journal of Geophysical Research*, 102(E2), 4045–4056. <https://doi.org/10.1029/96JE03320>
- Smith, M. D., Martínez, G. M., Sebastián, E., Lemmon, M. T., Wolff, M. J., Apéstitque, V., et al. (2023). Diurnal and seasonal variations of aerosol optical depth observed by MEDA/TIRS at Jezero Crater, Mars. *Journal of Geophysical Research: Planets*, 128(1), e2022JE007560. <https://doi.org/10.1029/2022JE007560>
- Smith, M. D., Wolff, M. J., Spanovich, N., Ghosh, A., Banfield, D., Christensen, P. R., et al. (2006). One Martian year of atmospheric observations using MER Mini-TES. *Journal of Geophysical Research*, 111(E12), E12S13. <https://doi.org/10.1029/2006JE002770>
- Soffen, G. A., & Snyder, C. W. (1976). The first Viking mission to mars. *Science*, 193(4255), 759–766. <https://doi.org/10.1126/science.193.4255.759>
- Soria-Salinas, Á., Zorzano, M.-P., Mantas-Nakhai, R., & Martín-Torres, J. (2020). Wind retrieval from temperature measurements from the rover environmental monitoring station/Mars Science Laboratory. *Icarus*, 346, 113785. <https://doi.org/10.1016/j.icarus.2020.113785>
- Spanovich, N., Smith, M. D., Smith, P., Wolff, M. J., Christensen, P. R., & Squyres, S. W. (2006). Surface and near-surface atmospheric temperatures for the Mars Exploration rover landing sites. *Icarus*, 180(2), 314–320. <https://doi.org/10.1016/j.icarus.2005.09.014>
- Spiga, A. (2021). Turbulence in the lower atmosphere of Mars enhanced by transported dust particles. *Journal of Geophysical Research: Planets*, 126(11), e2021JE007066. <https://doi.org/10.1029/2021JE007066>
- Stull, R. B. (1988). *An introduction to boundary layer meteorology*. Springer.
- Taylor, P. A., Catling, D. C., Daly, M., Dickinson, C. S., Gunnlaugsson, H. P., Harri, A. M., & Lange, C. F. (2008). Temperature, pressure, and wind instrumentation in the Phoenix meteorological package. *Journal of Geophysical Research*, 113(E3), E00A10. <https://doi.org/10.1029/2007/JE003015>
- Tillman, J. E. (1972). Indirect determination of stability, heat and momentum fluxes in the atmospheric boundary layer from simple scalar variables during dry unstable conditions. *Journal of Applied Meteorology and Climatology*, 11(5), 783–792. [https://doi.org/10.1175/1520-0450\(1972\)011<0783:tidosh>2.0.co;2](https://doi.org/10.1175/1520-0450(1972)011<0783:tidosh>2.0.co;2)
- Vasavada, A. (2022). Mission overview and scientific contributions from the Mars Science Laboratory Curiosity rover after eight years of surface operations. *Space Science Reviews*, 218(3), 14. <https://doi.org/10.1007/s11214-022-00882-7>
- Vasavada, A., Piqueux, S., Lewis, K. W., Lemmon, M. T., & Smith, M. D. (2017). Thermophysical properties along Curiosity's traverse in Gale Crater, Mars, derived from the REMS ground temperature sensor. *Icarus*, 284, 372–386. <https://doi.org/10.1016/j.icarus.2016.11.035>
- Whiteway, J., Daly, M., Carswell, A., Duck, T., Dickinson, C., Komguem, L., & Cook, C. (2008). Lidar on the Phoenix mission to Mars. *Journal of Geophysical Research*, 113(E3), E00A08. <https://doi.org/10.1029/2007HE003002>
- Wolff, M. J., Smith, M. D., Clancy, R. T., Spanovich, N., Whitney, B. A., Lemmon, M. T., et al. (2006). Constraints on dust aerosols from the Mars exploration rovers using MGS overflights and mini-TES. *Journal of Geophysical Research*, 111(E12), E12S17. <https://doi.org/10.1029/2006JE002786>
- Wu, Z., Richardson, M. I., Zhang, Z., Cui, J., Heavens, N. G., Lee, C., et al. (2021). Large eddy simulations of the dusty Martian convective boundary layer with MarsWRF. *Journal of Geophysical Research: Planets*, 126(9), e2020JE006752. <https://doi.org/10.1029/2020JE006752>
- Zent, A. P., Hecht, M. H., Hudson, T. L., Wood, S. E., & Chevrier, V. F. (2016). A revised calibration function and results for the Phoenix mission TECP relative humidity sensor. *Journal of Geophysical Research: Planets*, 121(4), 626–651. <https://doi.org/10.1002/2015JE004933>

- Zurita-Zurita, S., de la Torre Juárez, M., Newman, C. E., Viúdez-Moreiras, D., Kahanpää, H. T., Harri, A.-M., et al. (2022). Mars Surface Pressure Oscillations as precursors of large dust storms reaching Gale. *Journal of Geophysical Research: Planets*, 127(8), e2021JE007005. <https://doi.org/10.1029/2021JE007005>
- Zurita-Zurita, S., Escribano, F. J., Sáez-Landete, J., & Rodríguez-Manfredi, J. A. (2020). Denoising atmospheric temperature measurements taken by the Mars Science Laboratory on the Martian surface. *IEEE Transactions on Instrumentation and Measurement*, 70, 1–10. <https://doi.org/10.1109/TIM.2020.3034986>